JOURNAL OF BIOMEDICAL OPTICS 3(3), 304–311 (JULY 1998)

COMPUTER-ASSISTED INTRA-OPERATIVE MAGNETIC RESONANCE IMAGING MONITORING OF INTERSTITIAL LASER THERAPY IN THE BRAIN: A CASE REPORT

Nobuhiko Hata,[†] Paul R. Morrison,[†] Joachim Kettenbach,[†] Peter McL. Black,[‡] Ron Kikinis,[†] and Ferenc A. Jolesz[†]

[†]Department of Radiology and [‡]Department of Surgery, Brigham & Women's Hospital, Harvard Medical School, Boston, Massachusetts 02115

(Paper JBO-151 received June 17, 1997; revised manuscript received Dec. 14, 1997; accepted for publication Jan. 22, 1998.)

ABSTRACT

Hardware and software for a customized system to use magnetic resonance imaging (MRI) to noninvasively monitor laser-induced interstitial thermal therapy of brain tumors are reported. An open-configuration interventional MRI unit was used to guide optical fiber placement and monitor the deposition of laser energy into the targeted lesion. T1-weighted fast spin echo and gradient echo images were used to monitor the laser tissue interaction. The images were transferred from the MRI scanner to a customized research workstation and were processed intraoperatively. Newly developed software enabled rapid (27–221 ms) availability of calculated images. A case report is given showing images which reveal the laser–tissue interaction. The system design is feasible for on-line monitoring of interstitial laser therapy. © *1998 Society of Photo-Optical Instrumentation Engineers.* [S1083-3668(98)01503-2]

Keywords magnetic resonance imaging; interventional MRI; computer assisted surgery; CAS; surgery; minimally invasive surgery.

1 INTRODUCTION

Laser-induced interstitial thermal therapy (LITT) is a minimally invasive surgical technique for the treatment of solid tumors. LITT has long been a topic of research; studies have focused on application of the technique in a variety of normal tissue types and tumors *in vivo* and *in vitro*.[1–10] The technique involves the percutaneous introduction of an optical fiber through a needle; light delivered to the tissue is absorbed proximal to the tip and the heat generated creates a localized coagulative necrosis.

As the device is interstitial, the laser–tissue interaction occurs remotely from the operator/surgeon and is not visible as would be the case in an open surgical procedure. Monitoring and control of the treatment is needed. One solution has been through the use of radiologic imaging techniques such as magnetic resonance imaging (MRI) and ultrasound (US) which can provide images of the interaction.[2,7,11–24]

Radiologic imaging techniques offer: (i) accurate image-guided placement of the optical fiber(s) into the target; (ii) intra-operative imaging to monitor tissue changes as they occur; and (iii) feedback (i.e., images of acute thermal effects) by which dosimetry can be optimized by additional treatment or a repositioning of the fiber. These provide control of the location and spatial extent of the thermally effected area (i.e., ''treatment site,'' ''induced-lesion''). MRI has found considerable acceptance and the clinical experience (of image-guided LITT in the brain, head and neck, liver, and spine) at various centers has been reported.[25–34]

It is important that MRI has excellent resolution of soft tissue but it is as important that various ''types'' of MRI are temperature sensitive (i.e., the signal intensity on the image is a function of temperature).[35] Types of MR imaging can be characterized by the ''pulse sequence'' by which the images are obtained. MRI pulse sequences such as those providing T1-weighted (T1w) fast spin echo (FSE), diffusion-weighted, and chemical-shift imaging have been shown to be temperature sensitive.[11,13,36–38]

MRI can provide a noninvasive means by which to monitor LITT. MRI sequences now provide images on a time scale which is suitable for LITT, providing near real-time monitoring. As changes in technology enable MRI-guided LITT to be implemented on patients, the information in the images must be optimally displayed so as to best appreciate the laser effect and to speed procedures. During

Address correspondence to Nobuhiko Hata, MRI Division, Department of Radiology, Brigham and Women's Hospital, 75 Francis St., Boston, MA 02115; E-mail: noby@bwh.harvard.edu

1083-3668/98/$10.00 © 1998 SPIE

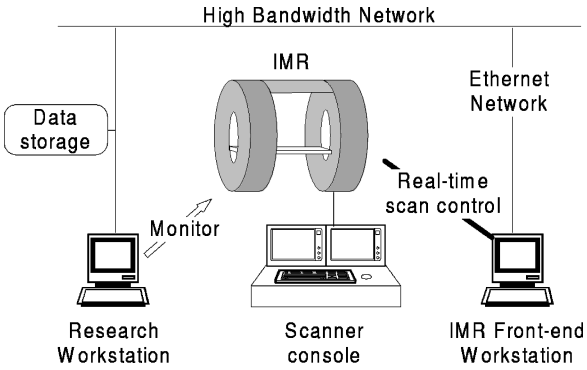

Fig. 1 The iMRI system is equipped with an iMRI workstation that communicates with a scanner and transfers real-time images to itself. A research workstation connected to the iMRI research workstation by Ethernet network performs ''temperature mapping'' (i.e., image subtraction) based on the images taken from the iMRI workstation. Calculated images from the research scanner can be displayed on LCD monitors at the surgical site.

Fig. 2 The open-configuration interventional MRI unit with 0.5 T superconducting magnets and 56 cm gap for surgical access provides a spherical imaging volume 30 cm in diameter. The scan plane can be determined by keyboard at a conventional console, or interactively determined by detection/localization system.

LITT changes in the images' signal intensity around the laser fiber's tip ranges from strong to subtle. This article presents the implementation of a research computer workstation to assist in the manipulation of image data to provide needed feedback as to the laser effect in a clinical setting. We report on one patient treated by LITT in the brain under both a T1w FSE and a water proton chemical shift imaging sequence for on-line monitoring of the intra-operative thermal effect.

2 MATERIALS AND METHODS

2.1 MR IMAGING

MR images were acquired using an ''open configuration'' interventional MRI (iMRI) unit (Signa SP, General Electric Medical Systems, Milwaukee, WI).[39] (See Figure 1.) The 0.5 T unit consists of upright coils spaced 0.56 m apart. The space allows a surgeon access to the patient while the anatomy is within the imaging volume (Figure 2). The MR images are displayed to the surgeon on liquid crystal displays (model LQ6NC01, Sharp Electronics, Rahwah, NJ) located above the surgical field. The iMRI system is well suited to provide good access to the patient while drawing trajectories to targeted tissue, inserting probes/needles under image guidance, and viewing images of the anatomy intraoperatively—all while the concerns of anesthesia, nursing, and sterility are met. To date, this system has been successfully applied to biopsies, tumor resections, and endoscopic surgeries.[40–46]

Two modes of scanning have been used: (1) conventional T1w FSE and (2) fast two-dimensional (2D) spoiled gradient recalled echo (2D-FSPGR). The T1w FSE has been cited to have a sensitivity of its signal intensity of 0.48%/°C (FSE, TR=300 ms, TE=12 ms) in a gel phantom.[36] The 2D-FSPGR, our water proton chemical shift sequence, has been reported to have a temperature sensitivity of -0.0135 ppm/°C.[37]

2.2 LASER DEVICE AND SETUP

The laser device (Sharplase 60, Sharplan Lasers, Allendale, NJ) emitted a continuous Nd:YAG laser at 1064 nm (nanometers). The laser light was transmitted into the procedure room through a long optical fiber passing through a port in the operating suite's magnet-shielded access panel. The long fiber passed the light into a connecting box (1-to-3 optical beamsplitter; Sharplan Lasers, Allendale, NJ). Up to three delivery fibers can be attached to the connecting box. The delivery fibers, which carry the light into the tissue, are bare, sterilized 600 μm fibers. The laser irradiation was performed at two positions in the tumor. The delivery fiber output was confirmed pre-operatively with an external power meter to be 4 W.

Positioning of the fibers in tissue was achieved using interactive scan plane definition by which an oblique image plane is determined using an optical scan-plane locator (Flashpoint, IGT Inc., Boulder, CO). This locator has three light-emitting diodes which are tracked by three charge coupled device (CCD) cameras attached to a gantry above the interventional field. The oblique scan plane can match an arbitrary plane for the trajectory of the needle into the tumor.

2.3 RESEARCH WORKSTATION

The iMRI unit is equipped with a dedicated workstation (Sun 4 model 670, Sun Microsystems, Mountain View, CA) by which the unit is run. We installed a second workstation (SPARCstation 20TZX model HS21, Sun Microsystems, Mountain View, CA) adjacent to the iMRI workstation. Our image processing computations were performed on this research workstation, since the hardware resources

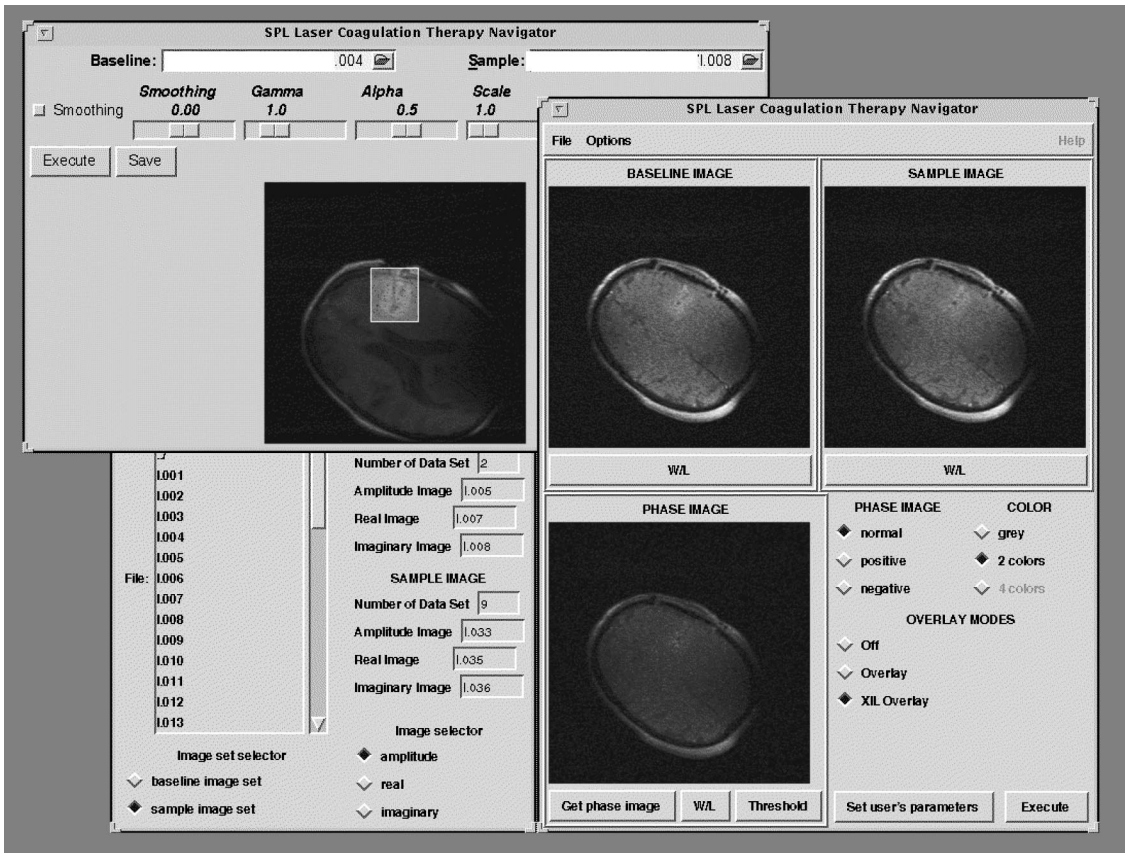

Fig. 3 Interactive control with graphical user interface for image mapping as displayed on the monitor of the research workstation.

of the MR workstation must be reserved for the image acquisition. The research unit was suitably capable of handling fast graphics manipulation and network communication needs. The research workstation had two separate display outputs each with its own graphics card: (1) a standard graphics card (TurboGX, Sun Microsystems, Mountain View, CA) to control the graphical user interface (Figure 3) which was connected to a monitor display (20 in. color monitor, Sun Microsystems, Mountain View, CA) placed in the iMRI control area, and (2) a card (TurboZX, Sun Microsystems, Mountain View, CA) which supports graphics acceleration and feeds the NTSC video signal to the two displays over the surgical field.

2.4 NETWORK

The iMRI unit, its workstation, and the research workstation used a standard TCP/IP protocol interface to establish network connection. Hosts were also connected to the hospital's network which connects existing research facilities, such as mass storage of pre-operative data (currently more than 180 GByte), connections to conventional MR/CT scanners and high end computing resources. However, the system presented in this article can operate independently, without access to these research facilities.

The network was based on switched Ethernet with a faster backbone, using high bandwidth asynchronous transfer mode (ATM). ATM bridges the switched Ethernet network, to which the research workstation belongs, and a second switched Ethernet based network, which contains the iMRI workstation. The data transfer speed is 10 Mbps in the switched Ethernet network and 155 Mbps in ATM. Therefore, each machine can achieve a maximum transfer rate of 10 Mbps. Typically, the data transfer time is 0.72 s for an image of $256\times256\times16$ bits.

2.5 SOFTWARE DEVELOPMENT

Figure 4 presents a schematic of the overall control flow. Server/client software was developed and installed in the iMRI workstation and the research workstation, respectively. This software distributed tasks by establishing a network communication by remote procedure control (RPC) and transferred commands and images between them.[47]

The iMRI server software is used to obtain image data from the scanner and send it to the research workstation. On request from the research workstation, the iMRI workstation allows access to its image buffer for transfer of the most recently acquired image to the research workstation. The image-to-buffer routine works independently of the server software and continuously refreshes its contents

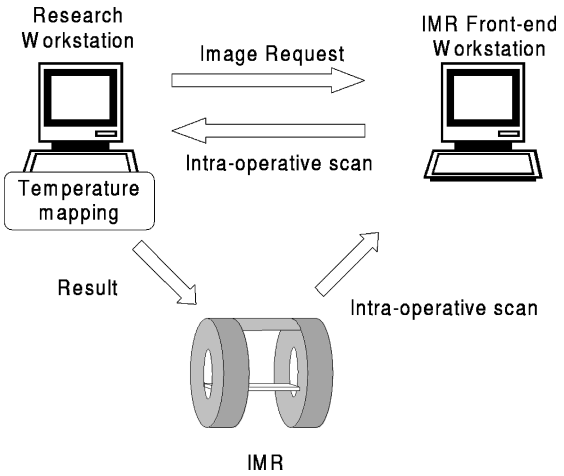

Fig. 4 Schematic representation of the control flow. When an image is requested by the research workstation, the iMRI workstation sends the latest image to the research workstation (0.72 s). The research workstation computes ''temperature'' maps (T1w FSE image difference: 27 ms; chemical shift mapping: 221 ms) and displays them on the monitors at the surgical field.

when the real-time scan is performed. This buffer is also shared with real-time image viewer and controller, which is installed in the iMRI workstation as the default interface.

The research workstation receives real-time images and processes them to provide a difference image to serve as a guide to the LITT procedure. This difference image can be routed for display to display screens above the surgical field.

Since the research workstation is dedicated specifically for 2D computer graphics, image processing, and its own customized user interface, its hardware is configured to maximize the performance of these functions. The iMRI workstation cannot achieve such optimization because of limited hardware resources that are designed only to maximize the performance of the real-time intra-operative image acquisition. The combination of a hardware-accelerated image processing library (XIL, Sun Microsystems, Mountain View, CA) and a compatible graphics board (Creator 3D, Sun Microsystems, Mountain View, CA) processed 2D images much faster in the research workstation than could be done in the iMRI workstation.[48] The accelerated image processing was provided by XIL and includes arithmetic, logic, geometric operations, convolutions, and image statistics. Benchmarking tests showed scaling and convolution functions to have performances of 2517 and 274 images/s (256×256 pixels×16 bits), respectively.

The development platform for the software used Task Command Language/Tool Kit (Tcl/Tk) with a combination of C/C++ languages.[49] Tcl/Tk is an integrated scripting language which not only has most of the capabilities of standard C/C++, but also supports socket level network communication, input-output (I/O) handling, looping, and mathematical manipulation. Tk is the extension of Tcl for

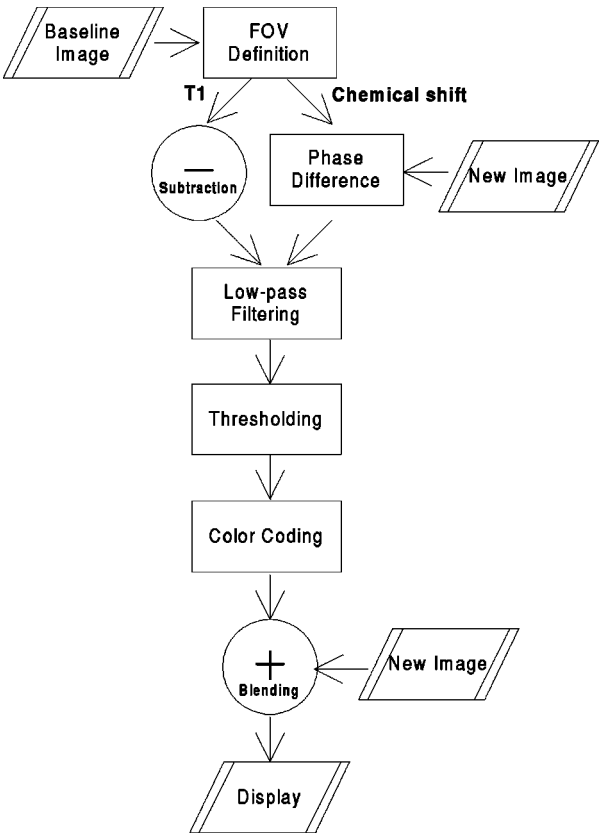

Fig. 5 Image processing to generate processed image using T1w FSE subtraction method or water proton chemical shift mapping. After calculating an output image, low-pass filtering and thresholding are applied to remove noise. Color coding is then applied to enhance the differences in signal intensity about the laser fiber's tip. This can be superimposed on a pre-laser baseline image.

graphical use interface construction which manages windows and mouse events.[50] One of the major benefits of Tcl/Tk is rapid prototyping and thus it is simple to develop interactive programs and graphical user interfaces.

Rapid prototyping was an important design decision essential for developing and refining the graphical user interfaces for a physician to use intra-operatively. Both Tcl and Tk have an interface which enables developers to implement custom C/C++ methods such as the two algorithms described below.

2.5.1 Algorithm 1: T1-Weighted FSE Image Subtraction

Intra-operatively acquired difference images provided by the research workstation were generated by subtracting and smoothing consecutive T1-w FSE MR images (Figure 5). The generation of the difference images centered around the subtraction of T1-w FSE images (256×256 pixels×16 bits) consisted of the sequential processes as described:

step (1) image acquisition; access to buffer; data transfer to research workstation;
step (2) FOV definition to enhance the region of interest;
step (3) image subtraction;
step (4) 3×3 low-pass Gaussian filtering for noise reduction;
step (5) user-defined thresholding to remove noise and enhance heated region;
step (6) color coding: red (hot) →Green (warm) →Blue (cool);
step (7) superimpose difference image onto original baseline image (as needed).

The computation time for steps (2)–(7) of the reconstruction process was 27 ms. Step (6) enhanced the visualization of the thermal effect by assigning a pseudo-color based on the values of the difference in the signal intensity from one image to another.

2.5.2 Algorithm 2: Water Proton Chemical Shift

Difference images were generated by subtracting and smoothing consecutive processed chemical shift MR images. The dependence of the water proton chemical shift on temperature is given by:

$$\Delta\phi = \tan^{-1}\left(\frac{\mathrm{Re}[S(T_B)]\cdot\mathrm{Im}[S(T)] - \mathrm{Re}[S(T)]\cdot\mathrm{Im}[S(T_B)]}{\mathrm{Re}[S(T)]\cdot\mathrm{Re}[S(T_B)] + \mathrm{Im}[S(T)]\cdot\mathrm{Im}[S(T_B)]}\right), \quad (1)$$

where $\Delta\phi$ is the phase distribution difference between the objective-temperature T image and the baseline-temperature Tb image.[37] S is the complex MR signal; Re and Im denote the real and imaginary parts, respectively.

The sequential procedure for providing the data intra-operatively for the calculated phase difference images (Figure 5) was nearly the same as shown above for the T1-w FSE images as input. However, here step (3) above was replaced by Eq. (1).

steps (1)–(2) (same as T1-weighted subtraction);
step (3) temperature map generation;
steps (4)–(7) (Same as T1-weighted subtraction).

The total computation time was 221 ms for Eq. (1), which is about ten times longer than a simple subtraction.

3 RESULTS

Patient (JA) was a 76-year-old female with a 2 cm high grade glioma in the left frontal lobe with resulting compression of the left lateral ventricle and midline shift. On the day of LITT, the patient was placed in the iMRI scanner. A clamp was used to fix the position of the head. After establishing a sterile field, a small 2–3 mm skin incision was made and a burr hole drilled through the skull and dura. Under MRI guidance, an MR-compatible sedan-type biopsy needle was placed in the mass and a diagnostic tissue sample (biopsy=positive) was taken. Again under MRI guidance, along the same needle path, the sterile laser delivery fiber was inserted into the tumor.

Laser irradiation was performed at two sites within the tumor. At each site, the laser was turned on three separate times, each time at an output of 4 W for a duration of 1 min.

Sequential images of the same tissue plane were obtained by an FSE sequence [TR/TE 400/18 ms, slice thickness 5 mm, field of view (FOV) 220 ×220 mm, matrix 256×128, 1 NEX] with acquisition time 7 s/image; the image plane was through the tip of the laser fiber in a plane perpendicular to it (Figure 6).

During a separate irradiation, sequential imaging was performed with the fast 2D-SPGR sequence [(TR/TE/flip angle 55/14 ms/20_i) with 4 mm slice thickness, FOV 320×240 mm, and a matrix of 256 ×128]. The magnitude, phase, real, and imaginary images were retrieved within 5–7 s for each slice. After measuring the water proton chemical shift change from the complex valued MRI signal, the results were displayed (Figure 6).

Post-operative MRI revealed the laser-induced lesion (Figures 7 and 8). Gray level distribution of the pre-, intra-, and post-operative images showed the matching of temperature increase and the lesion. Water proton chemical shift imaging had a steeper peak within the irradiation site than the T1-w FSE subtraction image.

4 DISCUSSION

Implementation of the software and hardware described above succeeded in monitoring the laser–tissue interaction. More than simply performing algebraic manipulations on the image data, however, data were provided as feedback at the time of surgery to the surgeon and radiologist. The interaction between the caregivers and the images was transacted through a user interface custom designed to facilitate the delivery of useful feedback. In this case, the feedback was in the form of the colorized image differences which highlighted the changes in the tissue during laser irradiation. The current version of the interface was operated by the programmer, but in the future, control would be handed to the imaging technologist, radiologist or surgeon on the case.

Integral to the implementation of a real-time feedback was the addition of a dedicated research workstation to the iMRI's own computing power. As detailed in Sec. II, the SUN SPARCstation was configured to maximize the performance of the requisite 2D computer graphics, image processing, and its user interface. The hardware of the iMRI workstation was designed to handle MR image acquisition. Importantly, the network connections allowed a reasonably fast image transfer time of 0.72 s; the feedback is needed in as near real-time as possible.

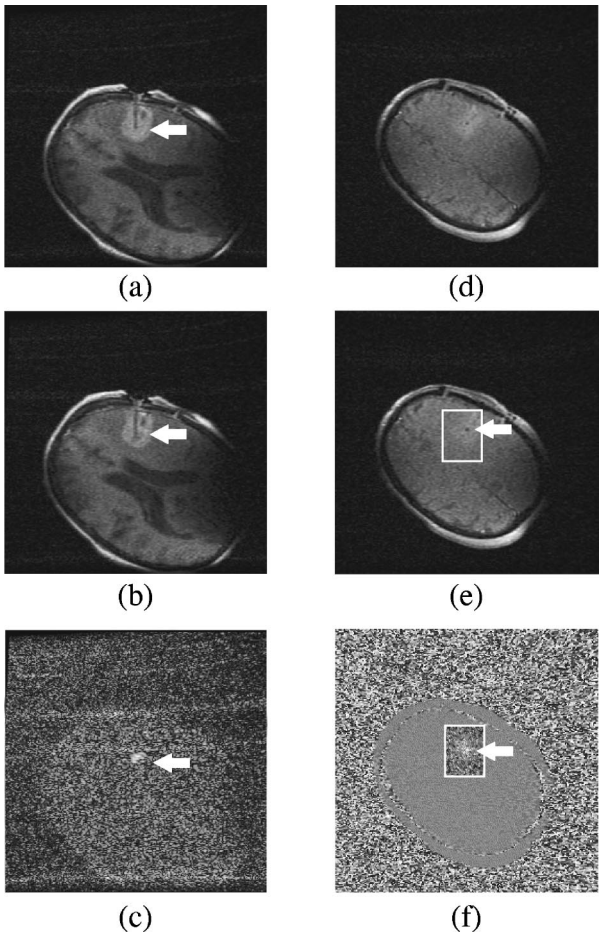

Fig. 6 Images from a case report on 76 year old female, glioma in the posterior left frontal lobe. On the left: T1-w FSE image subtraction. On the right: water proton chemical shift imaging. (a) T1w FSE image (axial, FSE, TR/TE 400/18 ms, slice thickness 5 mm, FOV 220×220 mm, matrix 256×128 pixels, 1 NEX) after the insertion of the guide needle. The white arrow indicates the target lesion and artifact of the guide. (b) T1w FSE image during the ablation. (c) Subtraction image [(b)–(a)] during the ablation. Note high contrast area at the tip of the white arrow around the laser tip. (d) A magnitude image from fast SPGR (TR/TE/flip angle 55/14 ms/20°, slice thickness 4 mm, FOV 320×240 mm, matrix 256×128) before coagulation. (e) Magnitude image from the fast SPGR during the coagulation. (f) Mapping with water proton chemical shift imaging. The intensity level in the black box is equalized for enhanced visibility. ''Temperature'' distribution is indicated by gray level in the box. The same is also indicated with a black box in (e).

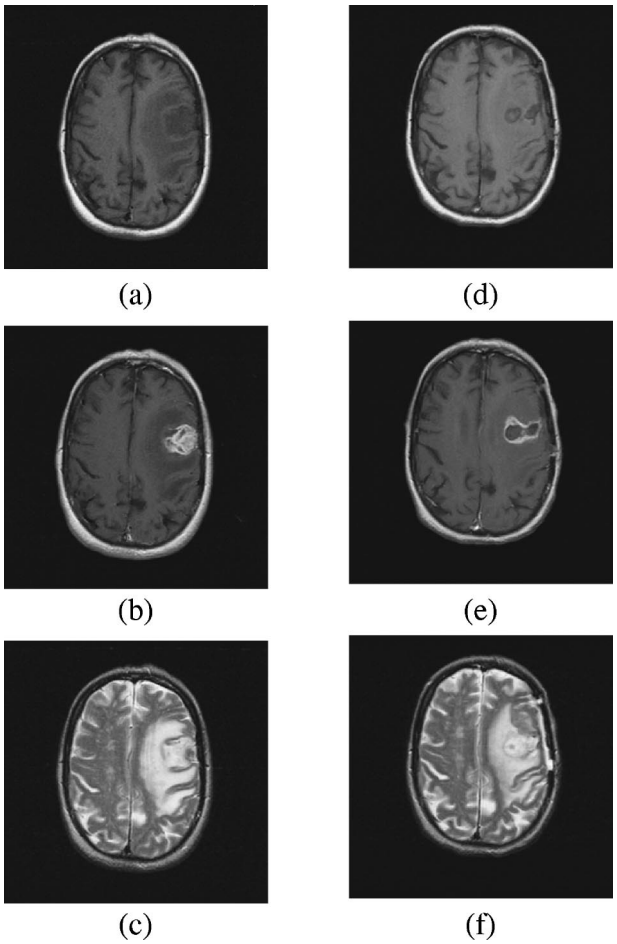

Fig. 7 Same case as in Figure 6: comparison of pre- and post-operative images. Pre-operative image: (a) T1-weighted image (axial, TR/TE 400/16 ms, slice thickness 5 mm, FOV 220 ×220 mm, matrix 256×192 pixels). A large alteration of intensity is noted in the left frontal and parietal regions with compression of the sylvian fissure. Associated with hypo-intense alteration of the adjacent white matter, a compression of the left lateral ventricle and slight middle shift is seen. (b) Gd-enhanced T1w image (TR/TE 500/16 ms) shows left hemispheric abnormality with a 3 cm area of contrast enhancement. (c) T2-weighted image (TR/TE 3000/95 ms). A significant hyperintense alteration of the white matter surrounds the tumor and extends into the frontal and parietal lobes. Post-operative images 3 days after the LITT. (d) T1-weighted image (TR/TE 400/16) indicates the two laser-induced lesions. Compared to the examination done before LITT, there is a decrease in size of the residual alteration of intensity in the left fronto-shaped area of max. 1.5 cm in diameter. (e) Gd-enhanced T1 (TR/TE 500/16 ms) showed no contrast enhancement at the center of the lesion, although there is an enhancing rim around the tumor site. (f) T2w image (TR/TE 3000/95 ms) has low intensity in the center of the tumor site and high intensity in the rim. The surrounding vasogenic edema has less compression of the left lateral ventricle.

(Recall that the calculations themselves are performed in less than 0.25 s.)

The current technique used a low-pass Gaussian filtering to highlight the regions of change in the MR signal. However, a simple median filter might be more successful at reducing speckle noise.[51] Alternatively, a more sophisticated edge-preserving smoothing operation could be employed.[52] The penalty for such filtering operations is computation cost, which will thus lengthen the interval between image-feedback updates. Another possible imaging method for navigation of LITT is optical flow analysis.[53] Based on the sequential images during laser irradiation, the optical flow analysis can predict the spread of thermal energy to adjacent tissues. In this way, interactive control of destructive deposition in every tissue is possible.

Although UNIX workstations and network facilities were utilized here to achieve real-time monitoring of LITT, this technology could also be ported to personal computers (PCs). Most of the commercially available PCs and their associated operating

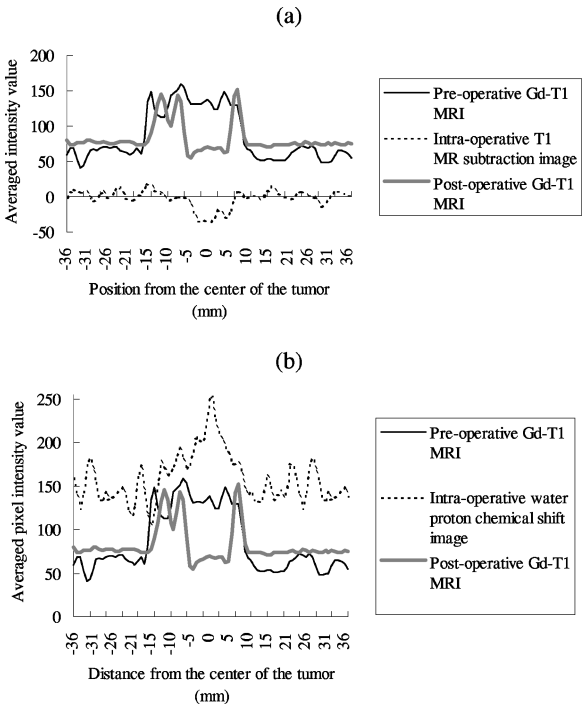

Fig. 8 (a) The signal intensity distribution around the tumor site from (1) pre-operative Gd-enhanced T1w image, (2) intra-operative water proton chemical shift image, and (3) post-operative Gd-enhanced T1 image. (b) The signal intensity distribution around the tumor site from (1) pre-operative Gd-enhanced T1w image, (2) intra-operative T1w MR subtraction image, and (3) post-operative Gd-enhanced T1w image. The center of the tumor site indicates the necrosis with intensity decrease in Gd-enhanced T1w images. It correlates well with the intensity increase in intraoperative water proton chemical shift image in (a) and the decrease in the T1-weighted MR subtraction image in (b).

system (e.g., Windows 95) already incorporate networking capabilities. The graphical user interface software also can be ported to a PC environment, as its architecture was carefully chosen to be run across platforms.

5 CONCLUSION

MRI offers a sensitive, noninvasive technology by which interstitial thermal therapies can be monitored and thereby controlled. The application of laser-induced coagulation for tumor therapy has been limited by the ability to monitor the laser–tissue interaction. Slow MRI image acquisition sequences and closed MRI scanners showed the promise of such treatments over the last decade. Now, fast imaging sequences and ''open'' interventional units deliver on this promise.

As research now looks to optimize the imaging sequences used, there are still important components of such therapies that must be tested and evaluated. A crucial component is the concept of feedback, which is the technological environment by which the feedback is provided. We provided a report on a system design feasible for on-line monitoring of interstitial laser therapy in the brain in a real, dedicated iMRI environment. We described the system's engineering aspects and shared data from clinical application in a patient.

Acknowledgments

Nobuhiko Hata was supported by a fellowship from the Japan Society for the Promotion of Science (JSPS). The authors thank Dr. Abhir Bhalerao and other colleagues of SPL, Brigham and Women's Hospital, Boston for their productive advice. They are also grateful for the contribution of Yoshikazu Nakajima of the University of Osaka. Ron Kikinis and Ferenc Jolesz were supported in part by NIH Grant No. P01-CA67165.

REFERENCES

1. K. Matthewson, P. Coleridge-Smith, J. P. O'Sullivan, T. C. Northfield, and S. G. Bown, ''Biological effects of intrahepatic neodymium: yttrium-aluminum-garnet laser photocoagulation in rats,'' *Gastroenterology* **93**, 550–557 (1987).
2. F. A. Jolesz, A. R. Bleier, P. Jakab, P. W. Ruenzel, K. Huttl, and G. J. Jako, ''MR imaging of laser-tissue interactions,'' *Radiology* **168**, 249–253 (1988).
3. G. Godlewski, S. Rouy, C. Pignodel, H. Ould-Said, J. J. Eledjam, J. M. Bourgeois, and P. Sambuc, ''Deep localized Nd:YAG laser photocoagulation in liver using a new water-cooled and echoguided handpiece,'' *Lasers Surg. Med.* **8**, 501–509 (1988).
4. K. Matthewson, H. Barr, C. Tralau, and S. G. Bown, ''Low power interstitial Nd-YAG laser photocoagulation, studies in a transplantable fibrosarcoma,'' *Br. J. Surg.* **76**, 378–381 (1989).
5. A. Masters and S. G. Bown, ''Interstitial laser hyperthermia in the treatment of tumors,'' *Lasers Med. Sci.* **5**, 129–135 (1990).
6. N. Daikuzono, S. Suzuki, H. Tajiri, H. Tsunekawa, M. Ohyama, and S. N. Joffe, ''Laserthermia: A new computer-controlled contact Nd:YAG system for interstitial local hyperthermia,'' *Lasers Surg. Med.* **8**, 254–-258 (1988).
7. A. H. Dachman, J. A. McGehee, T. E. Beam, J. A. Burris, and D. A. Powell, ''US-guided percutaneous laser ablation of liver tissue in a chronic pig model,'' *Radiology* **176**, 129–133 (1990).
8. R. Schober, M. Bettag, M. Sabel, F. Ulrich, and S. Hessel, ''Fine structure of zonal changes in experimental Nd:YAG laser-induced interstitial hyperthermia,'' *Lasers Surg. Med.* **13**, 234–241 (1993).
9. R. Matsumoto, A. M. Selig, V. M. Colucci, and F. A. Jolesz, ''Interstitial Nd:YAG laser ablation in normal rabbit liver: trial to maximize the size of laser-induced lesions,'' *Lasers Surg. Med.* **12**, 650–658 (1992).
10. J. Heisterkamp, R. van Hillegersberg, E. Sinofsky, and J. N. M. Ijzermans, ''Heat-resistant cylindrical diffuser for interstitial laser coagulation: comparison with bare-tip fiber in a porcine liver model,'' *Lasers Surg. Med.* **20**, 304–309 (1997).
11. A. R. Bleier, F. A. Jolesz, M. S. Cohen, R. M. Weisskoff, J. J. Dalcanton, N. Higuchi, D. A. Feinberg, B. R. Rosen, R. C. McKinstry, and S. G. Hushek, ''Real-time magnetic resonance imaging of laser heat deposition in tissue,'' *Magn. Reson. Med.* **21**, 132–137 (1991).
12. L. P. Panych, M. I. Hrovat, A. R. Bleier, and F. A. Jolesz, ''Effects related to temperature changes during MR imaging,'' *J. Magn. Reson. Imag.* **2**, 69–74 (1992).
13. R. Matsumoto, K. Oshio, and F. A. Jolesz, ''Monitoring of laser and freezing-induced ablation in the liver with T1-weighted MR imaging,'' *J. Magn. Reson. Imaging* **2**, 555–562 (1992).
14. N. Higuchi, A. R. Bleier, F. A. Jolesz, V. M. Colucci, and J. H.

Morris, ''Magnetic resonance imaging of the acute effects of interstitial neodymium:YAG laser irradiation on tissues,'' *Invest. Radiol.* **27**, 814–821 (1992).
15. M. Fan, P. W. Ascher, O. Schrottner, F. Ebner, R. H. Gemann, and R. Kleinert, ''Interstitial 1.06 Nd:YAG laser thermotherapy for brain tumors under real-time monitoring of MRI: Experimental study and phase I clinical trial,'' *J. Clin. Laser Med. Surg.* **10**, 355–361 (1992).
16. G. Godlewski, J. M. Bourgeois, P. Sambuc, C. Gouze, H. Ould-Said, J. J. Eledjam, S. Rouy, and C. Pignodel, ''Ultrasonic and histopathological correlations of deep focal hepatic lesions induced by stereotactic Nd:YAG laser applications,'' *Ultrasound Med. Biol.* **14**, 287–291 (1988).
17. D. E. Malone, D. R. Wyman, D. J. Moote, F. G. DeNardi, H. Mori, C. Swift, R. Lewis, G. W. Stevenson, and B. C. Wilson, ''Sonographic changes during hepatic interstitial laser photocoagulation,'' *Invest. Radiol.* **27**, 804–813 (1992).
18. D. E. Malone, D. R. Wyman, F. G. DeNardi, F. P. McGrath, C. J. De Gara, and B. C. Wilson, ''Hepatic interstitial laser photocoagulation: an investigation of the relationship between acute thermal lesions and their sonographic images,'' *Invest. Radiol.* **29**, 915–921 (1994).
19. R. van Hillegersberg, M. T. de Witte, W. J. Kort, and O. T. Terpstra, ''Water-jet-cooled Nd:YAG laser coagulation of experimental liver metastases: correlation between ultrasonography and histologic,'' *Lasers Surg. Med.* **13**, 332–343 (1993).
20. Z. Amin, J. J. Donald, A. Masters, R. Kant, A. C. Steger, S. G. Bown, and W. R. Lees, ''Hepatic metastases: Interstitial laser photocoagulation with real-time US monitoring and dynamic CT evaluation of treatment,'' *Radiology* **187**, 339–347 (1993).
21. R. A. Tracz, D. R. Wyman, P. B. Little, R. A. Towner, W. A. Stewart, S. W. Schatz, B. C. Wilson, P. W. Pennock, and E. G. Janzen, ''Comparison of magnetic resonances images and histopathological findings of lesions induced by interstitial laser photocoagulation in the brain,'' *Lasers Surg. Med.* **13**, 45–54 (1993).
22. T. Pushek, K. Farahani, R. E. Saxton, J. Soudant, R. Lufkin, M. Paiva, N. Jongewaard, and D. J. Castro, ''Dynamic MRI-guided interstitial laser therapy: A new technique for minimally invasive surgery,'' *Laryngoscope* **105**, 1245–1252 (1995).
23. M. P. Fried, P. R. Morrison, S. G. Hushek, G. A. Kernahan, and F. A. Jolesz, ''Dynamic T1-weighted magnetic resonance imaging of interstitial laser photocoagulation in the liver: observations on in vivo temperature sensitivity,'' *Lasers Surg. Med.* **18**, 410–419 (1996).
24. P. R. Morrison, F. A. Jolesz, D. Charous, R. V. Mulkern, S. G. Hushek, R. Margolis, and M. P. Fried, ''MRI of laser-induced interstitial thermal injury in an *in vivo* animal liver model with histologic correlation,'' *J. Magn. Reson. Imaging* **8**, 57–63 (1998).
25. M. Bettag, F. Ulrich, R. Schober, M. Sabel, T. Kahn, and W. J. Bock, ''Laser-induced interstitial thermotherapy in malignant gliomas,'' *Adv. Neurosurg.* **22**, 253–257 (1992).
26. M. Fan, P. W. Ascher, O. Schrottner, F. Ebner, R. H. Germann, and R. Kleinert, ''Interstitial 1.06 Nd:YAG laser thermotherapy for brain tumors under real-time monitoring of MRI: Experimental and phase I clinical trail,'' *J. Clin. Laser Med. Surg.* **10**, 355–361 (1992).
27. D. J. Castro, R. B. Lufkin, R. E. Saxton, A. Yerges, J. Soudant, L. J. Layfield, B. A. Jabour, P. H. Ward, and H. Kangarloo, ''Metastatic head and neck malignancy treated using MRI guided interstitial laser phototherapy: An initial case report,'' *Laryngoscope* **102**, 26–32 (1992).
28. C. P. Nolsoe, S. Torp-Pedersen, F. Burcharth, et al., ''Interstitial hyperthermia of colorectal liver metastases with a US-guided Nd:YAG laser with a diffuser tip: a pilot clinical study,'' *Radiology* **187**, 333–337 (1993).
29. T. Kahn, M. Bettag, F. Ulrich, H. J. Schwarzmaier, R. Schober, G. Fürst, and U. Mödder, ''MR-imaging guided laser-induced interstitial thermotherapy in cerebral neoplasm,'' *J. Comput. Assist. Tomogr.* **18**, 519–532 (1994).
30. B. Gewiese, J. Beuthan, F. Fobbe, D. Stiller, G. Müller, J. Böse Landgraf, K. J. Wolf, and M. Deimling, ''MRI-controlled laser-induced interstitial thermo-therapy of the liver,'' *Invest. Radiol.* **29**, 345–351 (1994).
31. T. Kahn, T. Harth, J. C. Kiwit, H. J. Schwarzmaier, C. Wald, and U. Mödder, ''*In vivo* MRI thermometry using a phase-sensitive sequence: preliminary experience during MRI-guided laser-induced interstitial thermotherapy of brain tumors,'' *J. Magn. Reson. Imaging* **8**, 160–164 (1998).
32. T. J. Vogl et al., ''Malignant liver tumors treated with MR imaging-guided laser-induced thermotherapy: technique and prospective results,'' *Radiology* **196**, 257–265 (1995).
33. T. J. Vogl et al., ''Recurrent nasopharyngeal tumors: Preliminary clinical results with interventional MR-imaging-controlled laser-induced thermotherapy,'' *Radiology* **196**, 725–729 (1995).
34. A. W. Schoenenberger, P. Steiner, J. F. Debatin, K. Zweifel, P. Erhart, G. K. von Schulthess, and J. Hodler, ''Real-time monitoring of laser diskectomies with a super-conducting open-configuration MR system,'' *AJR* **169**, 863–867 (1997).
35. H. E. Cline, J. F. Schenck, R. D. Walkins, K. Hynynen, and F. A. Jolesz, ''Magnetic resonance guided thermal surgery,'' *Magn. Reson. Med.* **30**, 98–106 (1993).
36. R. Matsumoto, R. V. Mulkern, S. G. Hushek, and F. A. Jolesz, ''Tissue temperature monitoring for thermal interventional therapy: Comparison of T1-weighted MR sequences,'' *J. Magn. Reson. Imag.* **4**, 65–70 (1994).
37. K. Kuroda, Y. Suzuki, Y. Ishihara, K. Okamoto, and Y. Suzuki, ''Temperature mapping using water proton chemical shift obtained with 3D-MRSI: Feasibility in vivo,'' *Magn. Reson. Med.* **35**, 20–29 (1996).
38. Y. Ishihara, A. Calderon, H. Watanabe, K. Okamoto, Y. Suzuki, K. Kuroda, and Y. Suzuki, ''A precise and fast temperature mapping using water proton chemical shift,'' *Magn. Reson. Med.* **34**, 814–823 (1995).
39. J. F. Schenck et al., ''Superconducting open-configuration MR imaging system for image-guided therapy,'' *Radiology* **195**, 805–814 (1995).
40. S. G. Silverman, B. D. Collick, M. R. Figueira, R. Khorasani, D. F. Adams, R. W. Newman, G. P. Topulos, and F. A. Jolesz, ''Interactive MR-guided biopsy in an open-configuration MR imaging system,'' *Radiology* **197**, 175–181 (1995).
41. T. M. Moriarty, R. Kikinis, F. A. Jolesz, P. M. Black, and E. Alexander, ''Intra-operative MR imaging,'' *Neurosurg. Clin. N. Am.* **7**, 323–331 (1996).
42. P. M. Black, T. Moriarty, E. Alexander III, P. Stieg, E. J. Woodard, P. L. Gleason, C. H. Martin, R. Kikinis, R. B. Schwartz, and F. A. Jolesz, ''Development and implementation of intraoperative magnetic resonance imaging and its neurosurgical applications,'' *Neurosurgery* **41**, 831–845 (1997).
43. M. P. Fried, L. Hsu, G. Topulos, and F. A. Jolesz, ''Image-guided surgery in a new magnetic resonance suite: preclinical considerations,'' *Laryngoscope* **106**, 411–417 (1996.
44. A. El-Ouahabi, C. R. G. Guttmann, S. G. Hushek, A. R. Bleiner, K. Dashner, P. Dikkes, P. M. Black, and F. A. Jolesz, ''MRI guided laser therapy in a rat malignant glioma model,'' *Lasers Med. Sci.* **13**, 503–510 (1993).
45. M. P. Fried et al., ''Endoscopic sinus surgery with MRI guidance: Initial patient experience,'' *Otolaryngol. Head Neck Surg.* (in press).
46. M. P. Fried, F. A. Jolesz, and P. R. Morrison, ''Image guidance with laser applications,'' *Otolaryngologic Clinics North America* **29**, 1063–1078 (1996).
47. S. W. Richard, *Unix Networking Programming*, Prentice–Hall Englewood Cliffs, NJ (1990).
48. *Solaris XIL1.1 Imaging Library Programmer's Guide*, Sun Soft Inc., Mountain View, CA (1993).
49. J. K. Ousterhou, *Tcl and the TK Toolkit*, Addison-Wesley, Reading, MA (1994).
50. A. Nye, *Xlib Reference Manual*, O'Reilly & Associates, Sebastopol (1990).
51. W. K. Pratt, *Digital Image Processing*, Wiley-Interscience, New York (1991).
52. W. T. Freeman and E. H. Adelson, ''The design and use of steerable filters,'' *Proc. IEEE Pattern Anal. Machine Intelligence* **13**, 891–906 (1991).
53. G. P. Zientara, P. Saiviroonporn, P. R. Morrison, M. P. Fried, R. Kikinis, and F. A. Jolesz, ''MRI monitoring of laser ablation using optical flow,'' *JMRI* (in press).